JOURNAL OF MATERIALS SCIENCE **37** (2002) 2857–2864

Interfaces and dislocation substructures in a Nb-Ti base alloy: influence of creep deformation

S. M. ALLAMEH
The Princeton Materials Institute and The Department of Mechanical and Aerospace Engineering, Olden St. Princeton, NJ 08558, USA

R. W. HAYES
Metals Technology, Inc., 19801 Nordhoff Street, Northridge, CA 91324, USA

E. A. LORIA
Reference Metals Company, 1000 Old Pond Dr., Bridgeville, PA 15017, USA

W. O. SOBOYEJO
The Princeton Materials Institute and The Department of Mechanical and Aerospace Engineering, Olden St. Princeton, NJ 08558, USA
E-mail: soboyejo@princeton.edu

This paper presents the results of an experimental study of interfaces and dislocation substructures in a Nb-Ti base alloy subjected to creep deformation at different stress levels. Particular attention has been paid to the orientation relationship between the b.c.c. structure matrix and the f.c.c. structure precipitate. A specific orientation relationship, namely: $[100]/(110)_M \| [220](111)_P$ (where M and P subscripts denote matrix and precipitate, respectively) was observed in the sample subjected to highest stress level. While the coincident site lattice model predicts a $(100)/(100) - 45^\circ$ relationship, the orientation relationship developed is more consistent with lock-in and invariant line models. The implications of the observed relationship are discussed for the strengthening of the solid solution alloy.

1. Introduction

The structure of interfaces and the evolution of dislocation substructures may contribute significantly to the deformation behavior of materials [1]. Furthermore, although some low-energy interfaces (such as twist boundaries in shape memory alloys) may facilitate deformation [2], it is more common for the preferred low energy interfaces to resist dislocation motion and give rise to strengthening [3]. Also, the preferred orientation relationships (OR) between coherent or semi-coherent precipitates and the matrix may result in improved resistance against interfacial sliding during creep deformation.

The microstructure and energy of interphase interfaces can be predicted by a number of models, including those based on geometry of interface and those based on calculations. Coincident site lattice (CSL) [4–6], invariant-line [7], and lock-in [8] models are examples of first tier, while the embedded atom method, EAM, is an example of the second tier. In this study, predictions of some of the geometrical models are compared with the actual orientations observed in a Ti-Nb-Ti alloy in various microstructural conditions: "undeformed" but exposed to elevated temperatures, deformed in creep at low-stresses, and deformed in creep at high-stresses. The implications of the observed interfacial and dislocation substructures are then discussed.

2. Materials and microstructure

A multi-component, body centered cubic (b.c.c.) solid solution (44Nb-35Ti-6Al-5Cr-8V-1W-0.5Mo-0.3Hf-0.5O-0.3C) alloy, was examined in this study. The mechanical properties of the Nb-Ti base alloy have been studied extensively in prior work [9]. The alloy has high room temperature strength (~1000–1200 MPa), strength retention (strength decreases only by ~35% up to 704°C), moderate fracture toughness (~35 MPa$\sqrt{\text{m}}$) and fatigue crack growth resistance [9, 10]. It was produced by Reference Metals Company, Bridgeville, PA, using conditions that are summarized in Ref. [9]. A fully recrystallized microstructure was achieved by heat treating the as-received material for one hour at 1200°C. The heat treatment was carried out in a vacuum of $\sim 10^{-4}$ Torr.

The microstructure of the multi-component alloy is presented in Fig. 1. The as-extruded Nb-Ti base alloy had a Van Gogh Sky-type (VGS) microstructure (Fig. 1a) [11]. After recrystallization at 1200°C for 1 hour a more homogeneous microstructure was formed

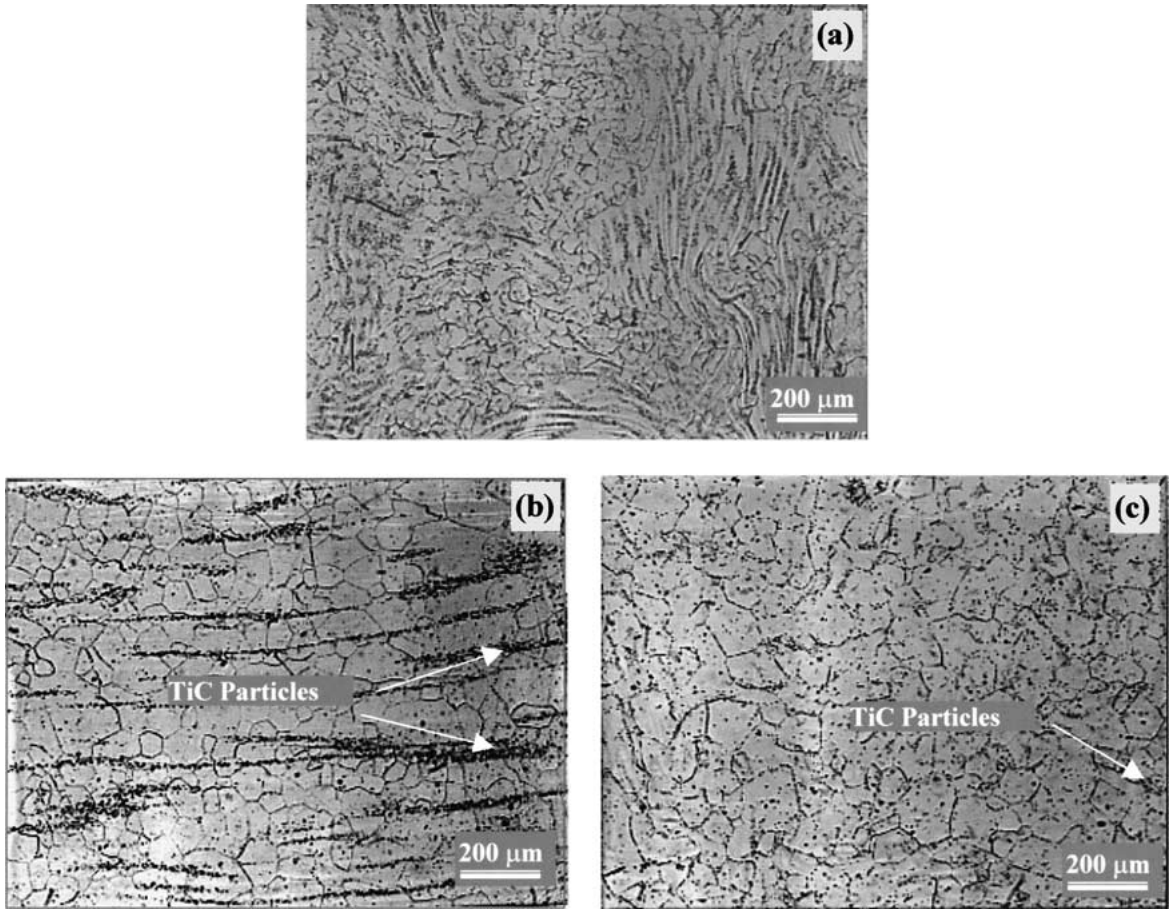

Figure 1 (a) VGS microstructure of the as-received material (b and c) recrystallized microstructure after heat treatment at 1200°C for 1 hr, (b) Longitudinal cross-section and (c) transverse cross-section.

(Fig. 1b). However, stringers of TiC particles were also observed in the longitudinal section of the sample. These had a vertical separation of about 50–60 μm (Fig. 1b). The transverse section of the specimen, however, did not exhibit such stringers (Fig. 1c).

3. Experimental procedures

Cylindrical creep samples (6.25 mm gage length $\times$6.25 mm gage diameter) were subjected to tensile creep testing at Metals Technology Inc., Northridge, CA. Testing was performed in air at 704°C. Creep testing was conducted at stress levels between 69 and 172 MPa under constant load conditions. The tests were continued until the tertiary creep regime was reached. Gauge displacement was measured using a linear voltage displacement transducer (LVDT) attached to the load train. After testing, the samples were cooled under load to preserve the creep deformations substructures.

Transmission electron microscopy (TEM) was used to examine the microstructures, dislocation substructures and interfaces in the samples crept under tensile loading conditions at stress levels of 103 and 172 MPa at a temperature of 704°C. The gauge sections (deformed parts of the specimens) and the grip sections (undeformed parts) were sliced into 200 mm-thick foils by electro-discharge machining (EDM). Disks of 3-mm diameter, cut out of these foils, were polished, dimpled and ion milled to electron transparency at 6 kV. These foils were examined in a Phillips CM-200 transmission electron microscope (TEM) operated at 200 kV.

4. Results and discussion

4.1. Creep deformation

Creep curves obtained from samples (with recrystallized microstructure produced by heat treatment for 1 h at 1200°C) and at fixed stress levels of 69–138 MPa are presented in Fig. 2a. Magnified portions of the curves, revealing details of the primary, and secondary creep regimes, are presented in Fig. 2b. The latter figure shows an inverted primary creep behavior for some specimens, including those tested at 90 and 103 MPa. Fig. 3 shows the secondary creep rates corresponding the mean stresses presented in Fig. 2. The change in the slope is consistent with a transition from diffusion-controlled creep at low stress levels to dislocation controlled creep at higher stress levels [3].

4.2. Dislocation sub-structures

A bright field (BF) transmission electron image of the "undeformed" sample is shown in Fig. 4. A selected area diffraction pattern (SADP), with major reflections labeled, is presented as an insert. This was done to show the two-beam diffraction condition for the BF image. No particular orientation relationship was observed between the matrix and precipitates. Also, the dislocation density was relatively low in the "undeformed" condition.

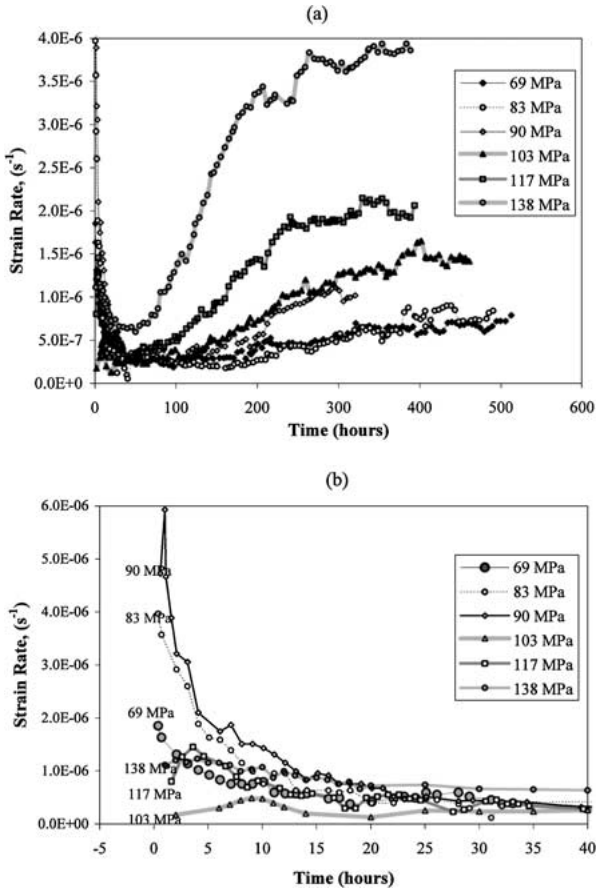

Figure 2 (a) Creep rates obtained for different stress levels, (b) Magnified view of primary and secondary creep regimes.

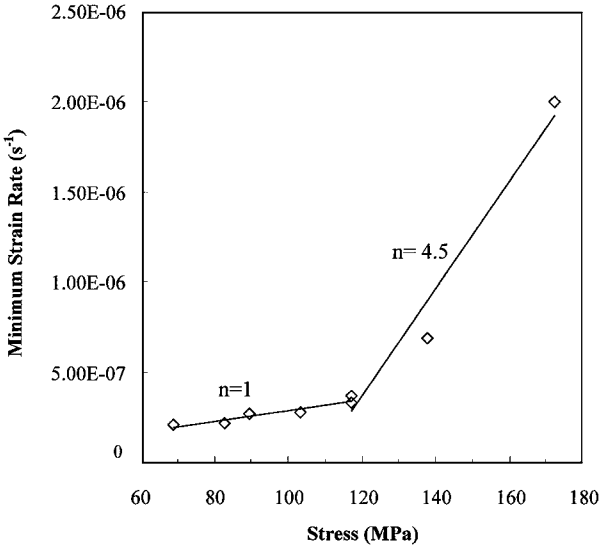

Figure 3 Minimum creep rates versus applied (mean) stress for multicomponent Nb-Ti base alloy tested at 704°C.

Transmission electron micrographs of the deformed specimens (crept at 103 MPa) are presented in Figs 5 and 6. The SADP insert shows the diffraction conditions. A part of the image that shows a bowed dislocation is blown up as a second insert to show the curvature of the bowing dislocation. Two TiC particles are observed interacting with the dislocations. These are identified with arrows in Fig. 5. The particle sizes are between 200–500 nm. Clear evidence of creep deformation substructures is observed in this figure. A range of dislocation morphologies was observed in various

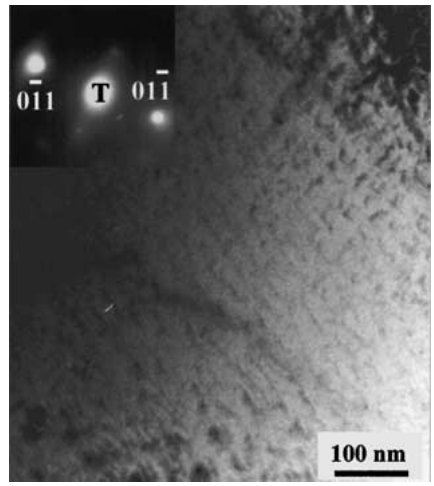

Figure 4 Bright field (BF) image of undeformed specimen under diffraction conditions shown in the selected area diffraction pattern (SADP) insert with major reflections labeled.

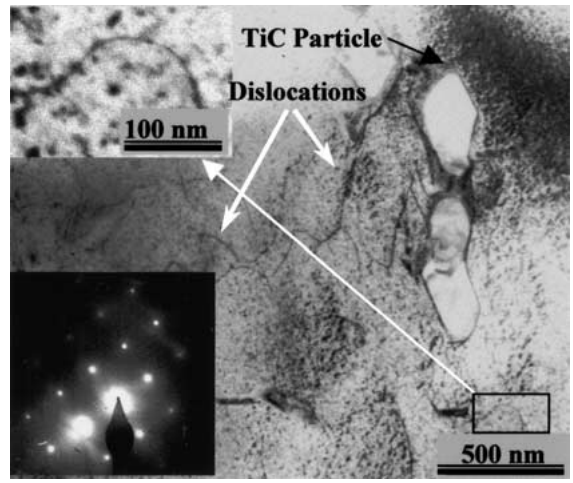

Figure 5 BF image of the specimen deformed at a temperature of 704°C and a stress level of 103 MPa. A magnified image of a bowing dislocation along with SADP is included as inserts.

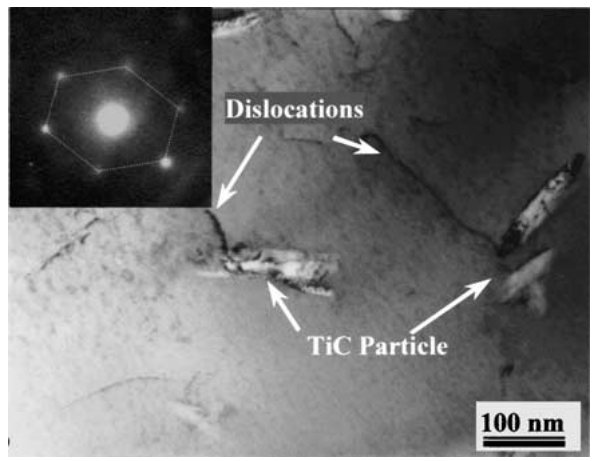

Figure 6 BF image of specimen showing dislocation/particle interaction. A SADP is included to show diffraction condition.

regions of the sample crept at 103 MPa. No dominant type dislocation was observed.

Evidence of dislocation grazing [12, 13] was observed in sample crept at 103 MPa. Dislocations were seen to graze the side of the TiC particles (Fig. 6). This is true for particles with incoherent boundaries where dislocations moving on slip planes intersecting

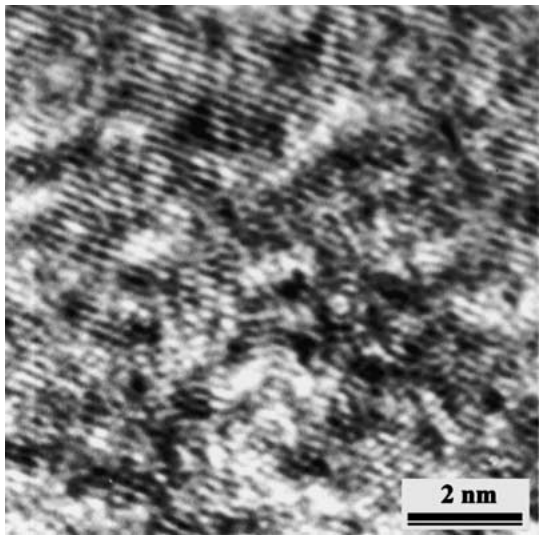

Figure 7 BF images of matrix of the specimen deformed at 103 MPa. The long-range order is disturbed by the presence of precipitates/impurities.

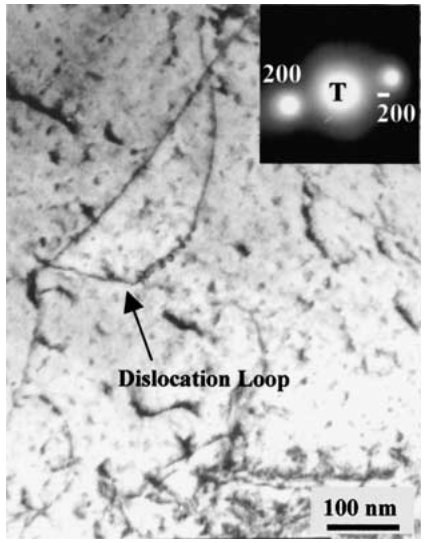

Figure 8 BF images of matrix of the specimen deformed at 172 MPa. Dislocation bowing is clearly observed. SADP insert shows diffraction condition.

the particle are attracted to the particle [12, 13]. Since TiC particles have higher moduli than the Nb-Ti base matrix, the attraction of the dislocations to the TiC particle boundaries is only energetically favored when the modulus mismatch stresses or misfit stresses due to the thermal expansion mismatch between TiC and the "matrix" alloy are relaxed by diffusion [12, 13]. In oxide-dispersion-strengthened alloys, the detachment of grazing dislocations from dispersed particles has also been shown by Rössler and Arzt [14] to give rise to the so-called threshold stress effect. However, no threshold stress effect has been observed, so far, in the multi-component Nb-Ti base alloy tested over a range of mean stresses between 69 and 172 MPa.

To evaluate the effect of high stress levels on the microstructure, thin foils made from a specimen deformed at a stress level of 172 MPa and a temperature of 704°C were examined in the TEM. Fig. 7 shows a BF image of the matrix displaying dislocation loops similar to those observed for the specimen deformed at 172 MPa. A labeled diffraction pattern is inserted to show the diffraction conditions. Bright field (BF) images of particles and corresponding diffraction patterns are presented in Fig. 8.

4.3. Interfaces and orientation relationships

It is interesting to investigate the possibility of a preferred orientation relationship (OR) between the matrix and the precipitates. Based on the results of this and previous studies [15], the solid solution matrix has a b.c.c. structure with a lattice parameter of 0.33 nm. On the other hand, metal carbide precipitates detected and examined in the matrix, after recrystallization heat treatment, have an f.c.c. structure with a lattice parameter of about 0.45 nm [15]. The lattice periodicity of the b.c.c matrix in [220]-type direction is 0.46 nm. This is close to that of the precipitate in [200]-type direction. Also the lattice spacing of the f.c.c. precipitate in the [220]-type direction is about 0.32 nm, which is close to that of matrix in [200]-type direction. This means that atomic rows of the two crystals (matrix and precipitates) will match when [220] of either crystal becomes parallel to [200] of the other crystal at the interface.

The misfit parameter, defined as $(a_M - a_P)/a_M$ would be ∼3% for $[200]_M \| [220]_P$. Subscripts M and P represent b.c.c matrix and f.c.c. precipitate respectively and a represents the lattice spacing in a given crystallographic orientation. As expected from geometrical models, an orientation relationship could develop during precipitation or upon annealing/deformation of the alloy. The simplest orientation relationship that can develop is cube-on-cube, with a 45° twist angle to bring the [220]-type direction of matrix parallel to [200]-type direction of the precipitate. In this OR, called the Bain orientation, the misfit is exactly the same in the two orthogonal directions (∼3%), resulting in an excellent near coincidence of $\Sigma 1/\Sigma 1$ with every lattice site coincident.

In order to examine the orientation relationship between the particles and the matrix, bright field (BF), dark field (DF) images and the corresponding selected area diffraction patterns (SADP) of the particle are presented in Figs 9a–c. These show that the particles are

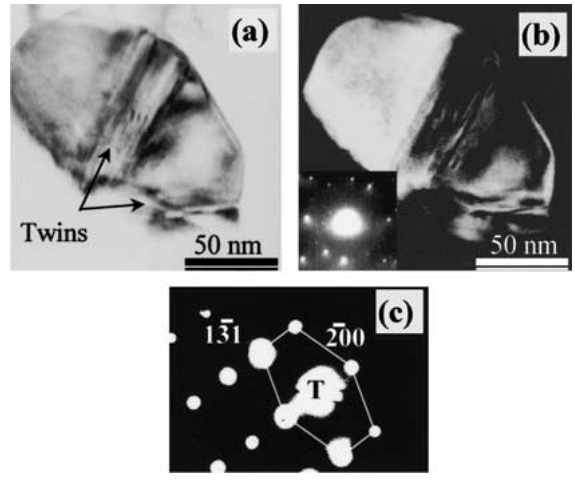

Figure 9 Bright field (BF) and dark field (DF) images of TiC particle (a) BF and (b) DF with a SADP included for diffraction condition, and (c) Selected area diffraction pattern from a TiC particle with major reflections labeled.

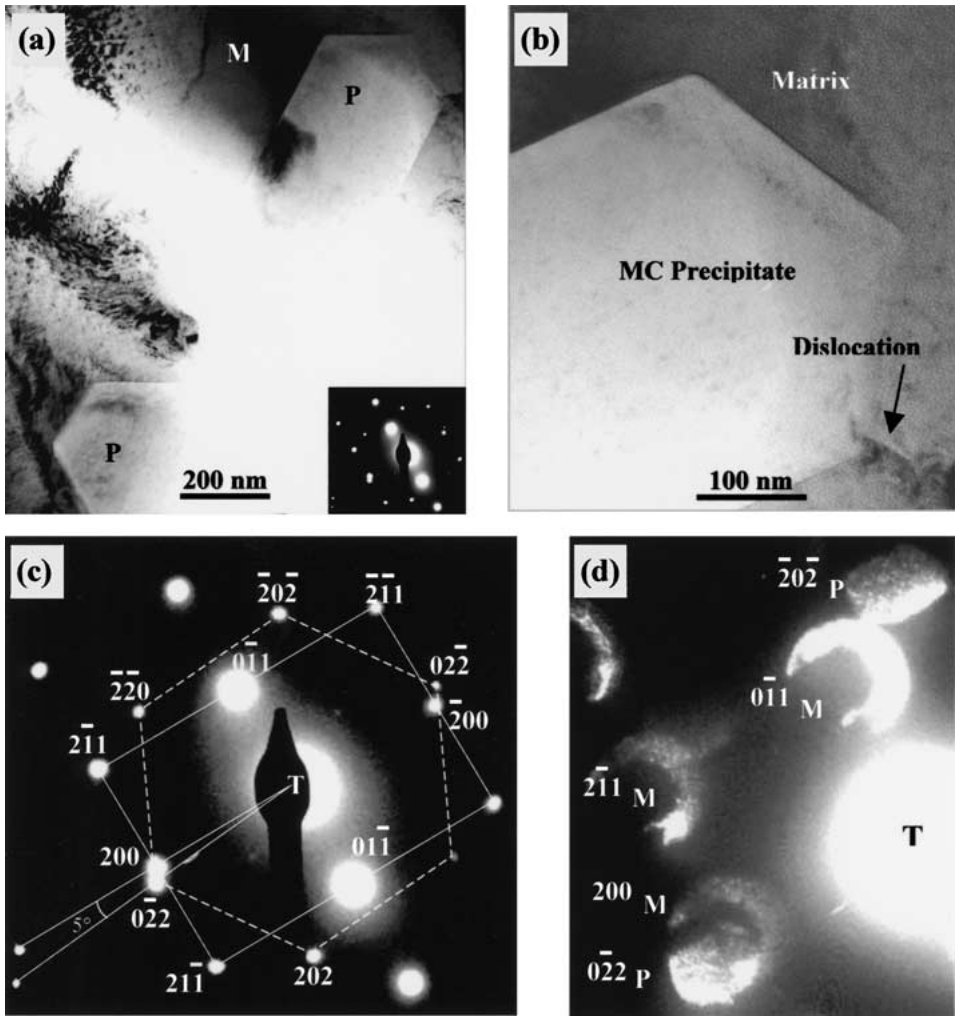

Figure 10 TEM analysis of the orientation relationship between TiC precipitates and the Nb-Ti base alloy, (a) BF image of carbides and matrix with an inserted diffraction pattern, (b) Higher magnification picture of precipitate showing hexagonal shape, (c) Indexed diffraction patterns of matrix (rectangular lattice, b.c.c structure) superimposed on diffraction pattern of precipitates (hexagonal f.c.c. structure), (d) Defocused diffraction spots of matrix (labeled *M*) and precipitate (labeled *P*) exhibiting the shape of matrix as dark (matrix spot) and bright (precipitate spot) as an elongated hexagon.

twinned, leading to corresponding diffraction patterns for more than one orientation. A diffraction pattern from a single particle is labeled and presented in Fig. 9c.

A high magnification TEM image of the matrix is shown in Fig. 7. In the lower half of the image, there are clusters of material that locally disturb the long-range order of the matrix crystal. The size of these clusters is a few atomic spacings, far less than the precipitate sizes studied here. Due to the small size of these clusters, evaluation of their composition and crystal structure needs further work that is beyond the scope of this paper. In any case, the exact role of these clusters in the strengthening of the matrix is yet to be fully resolved. However, since most crystal defects can act as barriers to dislocation motion, it is anticipated that these clusters contribute to the strength of the material.

A BF image of an area of sample deformed at 172 MPa and a temperature of 704°C is presented in Fig. 10. This shows two hexagonal-shaped precipitates (the one at the top right is elongated). As an insert in the bottom left corner of the image, a selected area diffraction pattern (SADP) is presented to show the imaging conditions.

To further elaborate the shape of the precipitates, the lower precipitate is enlarged in Fig. 10b. Dislocation interactions with this particle are observed at the bottom of the precipitate. An enlarged image of the SADP, with major reflections belonging to the matrix and precipitate indexed, is presented in Fig. 10c. The reflections belonging to f.c.c. matrix have a hexagonal pattern ($\bar{1}$ 11), as shown by the dashed hexagon with indexed $\langle 220 \rangle$ reflections. On the other hand, the b.c.c. matrix has a rectangular diffraction pattern of (011) zone with the longer side leading to (200) spot and shorter side leading to ($0\bar{1}1$) spot. It is clearly seen from the proximity of the ($\bar{2}00$) reflection of matrix to the ($02\bar{2}$) of the precipitate that the two directions are nearly parallel. There is a small relative twist between the two crystals, namely the misorientation angle is about 5 degrees.

In order to illustrate the source of various reflections being either matrix or precipitates, the diffraction pattern of Fig. 10c was defocused and presented in Fig. 10d. Two major reflections that nearly coincide show the precipitate or matrix. These are (200) of matrix and ($0\bar{2}2$) of precipitate. The particle is dark in the matrix spot, while the matrix is bright, and conversely, the precipitate is bright in the precipitate spot, while the matrix is dark. The slight shift downward is quite clear from the two diffracted spots.

As discussed earlier, the lattice periodicity in the [200]-type direction of b.c.c. matrix is about 0.33 nm. For the [220]-type direction of the f.c.c. precipitate, the lattice periodicity is about 0.32 nm. The misfit between these matrix and precipitate periodicities is about 3%. This may explain why these two directions are near parallel at the matrix/precipitate interface. The directions perpendicular to these, however, are associated with a misfit of −19% for 1 : 1 matching. This reduces to about 1% for a 5 : 6 matching. Coupling this 5 : 6 matching with a 1 : 1 matching in the other direction yields $\Sigma 5 : \Sigma 6$ with strains of about 3% or less. It is interesting that this orientation is preferred over $(001)/(001) - 45^\circ$ twist discussed earlier ($\Sigma 1 : \Sigma 1$), as evidenced from the results of the transmission electron microscopy.

4.4. Interface geometry and geometrical models

To explore some of the factors that lead to the preference for this close-packed plane interface, as opposed to the $(001)/(001) - 45^\circ$ interface, the interface geometry was evaluated in terms of predictions of geometrical models that describe the interfaces. For the $(001)/(001) - 45^\circ$ orientation, the atomic sites in the close-packed interface are all in near-coincidence ($\Sigma 1 : \Sigma 1$). However, the atomic plane spacings of the neighboring layers at the two sides of the interface are not equal. For the f.c.c. structure, the spacing of the layer adjacent to the interface is ∼0.25 nm, while similar spacing of the b.c.c. crystal is ∼0.16 nm. The energy contribution to the interface, from these two differently spaced layers, will be different.

For the observed OR, the interplanar spacings for the atomic planes at the two sides of the interface are ∼0.30 nm for the matrix, and ∼0.26 nm for the precipitate. The larger distance of the neighboring atomic planes, and the smaller difference between their spacing in the observed orientation may contribute to the preference of the close-packed interface observed for this alloy. Moreover, there is a chemical contribution from a variety of atoms in the matrix, namely Nb, Ti, Al, and to a lesser extent, other elements. This chemical component may also alter the energetics of the interface to the point where $(001)/(001) - 45^\circ$ orientation relationship becomes unfavorable.

The predictions of the invariant line model in terms of misorientation angle for the $(110)_M/(111)_P$ interface were examined for comparison with the observed OR. The invariant line forms an angle with the $[\bar{2}00]$ of matrix crystal, θ, and $[02\bar{2}]$ of the precipitate ϕ. As shown in the appendix, for this interface, these two angles are 2.46° and 2.92° respectively. The misorientation angle is the difference between these two angles, namely 0.46°. The misorientation angle predicted by the invariant line model (0.46°) shows a small deviation from exact parallelism of the closed pack rows in the two crystals. Although this does not explain the greater deviation from exact coincidence of atomic rows observed here (5° quantitatively), nevertheless, it justifies its presence. It must be noted that the driving force for reorientation of the precipitates to acquire coincident boundaries will decrease as the misorientation angle decreases and full coincidence may never realistically be reached.

4.5. Implications

The implications of the observed interfacial and dislocation substructures are very significant. First, the dislocation substructures indicate that creep strengthening may occur by a range of mechanisms. At low stresses (103 MPa), the dislocation/particle interactions suggest that dislocation bowing/Orowan looping (Fig. 5) and dislocation grazing (Fig. 6) are the dominant strengthening mechanism. Similarly, at higher stresses (∼172 MPa) dislocation bowing is still a dominant source of strengthening (Fig. 8). However, there is also a higher density of individual dislocations at the higher stress level.

Since the particle sizes are relatively small, the possible contributions from grain boundary sliding (to the overall/global deformation) are thought to be relatively small. However, the interfacial geometry and misfit strains are likely to have a strong effect on local particle deformation and dislocation/particle interactions. In the case of the TiC particles, the relatively high misfit strains (∼3–27%) appear to trap interacting dislocation segments at the particle boundaries. Furthermore, due to the misorientations between the matrix and the TiC particles, subsequent dislocation motion is associated with the bowing of pinned dislocations (Figs 5 and 8).

At the higher stress of 172 MPa, a higher density of unpinned individual dislocations was observed along with bowed dislocations that were pinned by TiC particles (Fig. 8). No evidence of grazing dislocations (Fig. 6) was observed in this regime. This suggests that the dislocations became detached during deformation at higher stresses. In an effort to support this claim, the detachment stress, σ_c was estimated for the grazing dislocation shown in Fig. 6. This was estimated from:

$$\sigma_c = \frac{Gb}{2\pi L}\left[2 + \ln\frac{r}{r'}\right] \quad (1)$$

where G is the shear modulus of the lattice, b is the magnitude of Burgers vector, L is the average separation of the pinning particles (the unbowed length of the dislocations), r is the interacting particle radius and r' is the dislocation core radius. The computed detachment stress is ∼173 MPa. This is comparable with the applied higher stress of 172 MPa, and consistent with dislocation-controlled creep mechanism with a creep exponent, n, of ∼4.5, which was obtained at higher stresses in this study (Fig. 3). In contrast, the creep exponent, $n = 1$, obtained at lower stresses, suggests a mechanism of diffusion controlled [16–18] or Harper-Dorn creep [19] at lower stresses. The pinning of dislocations provided by the TiC particles at lower stresses, therefore, appears to be sufficient to induce a transition to different creep deformation mechanisms at lower stresses.

5. Summary and conclusions

The interfacial geometries and dislocation substructures associated with creep deformation have been studied in a multi-component Nb-Ti based alloy deformed

in creep at 704°C. Salient conclusions arising from this work are summarized below.

1. Dislocation/TiC interactions occur during creep deformation at 103 MPa. These give rise to dislocation grazing and Orowan looping during deformation at the lower stress of 103 MPa. In contrast, a higher density of individual dislocations is observed at the higher stress of 172 MPa, along with bowed dislocations that are pinned by TiC particles.

2. The pinning of the dislocation segments is attributed to the high misfit strains (3–27%), and to a lesser extent, to the small twist misorientations between the TiC particles and the Nb-Ti base matrix.

3. The current study suggests that the dislocation/TiC particle interactions are sufficient to ensure that dislocation glide is not rate controlling in the lower stress regimes (103 MPa). However, at higher stress levels (172 MPa), the applied stresses are sufficient to detach the dislocations from the grazing configurations. Hence, a higher density of unpinned individual dislocations was observed at the higher stress level of 172 MPa. This is associated with a secondary exponent, n, of 4.5, which is consistent with a dislocation glide-controlled creep mechanism.

4. A preferred orientation relationship was observed between Nb-Ti base matrix and the TiC particles. Instead of a $(100)/(100) - 45^\circ$ orientation relationship predicted by CSL model, the observed orientation relationship of $[100]/(110)_M \| [220](111)_p$ is consistent with lock-in and invariant line models. The presence of preferred orientations between the matrix and precipitates may affect particle/dislocation interactions contributing to the strength of the material. The preferred orientation relationships (OR) between coherent or semi-coherent precipitates and the matrix may result in improved resistance against interfacial sliding during creep deformation.

Appendix

Invariant line model predicts the presence of preferred orientations based on the presence of an invariant line in the interface. Defined as a line whose length would remain unchanged during a transformation, which takes it from the matrix lattice ($\underline{\underline{S}}_M$) to the precipitate lattice ($\underline{\underline{S}}_P$), invariant line direction in the two crystals can be calculated following Boyne [20]:

$$\underline{\underline{S}}_P = \underline{\underline{A}}\,\underline{\underline{S}}_M \tag{A1}$$

If the vector $\vec{r}_1$ remains undeformed during transformation to $\vec{r}_2$ then

$$[r_1]^2 - [r_2]^2 = 0 \tag{A2}$$

and

$$\vec{r}_2 = \underline{\underline{A}}\vec{r}_1 \tag{A3}$$

For the interface between $(110)_M$ and $(111)_P$, the two matrices become 2-dimensional:

$$\underline{\underline{S}}_P = \begin{bmatrix} a_P\frac{\sqrt{2}}{2} & a_P\frac{\sqrt{2}}{4} \\ 0 & a_P\frac{\sqrt{6}}{4} \end{bmatrix} \tag{A4}$$

$$\underline{\underline{S}}_M = \begin{bmatrix} a_M & 0 \\ 0 & a_M\frac{\sqrt{2}}{2} \end{bmatrix} \tag{A5}$$

$$\underline{\underline{A}} = \underline{\underline{S}}_P[\underline{\underline{S}}_M]^{-1} = \frac{1}{a_M^2}\begin{bmatrix} a_P\frac{\sqrt{2}}{2} & a_P\frac{\sqrt{2}}{4} \\ 0 & a_P\frac{\sqrt{6}}{4} \end{bmatrix}\begin{bmatrix} a_M & 0 \\ 0 & a_M\sqrt{2} \end{bmatrix} \tag{A6a}$$

$$\underline{\underline{A}} = \begin{bmatrix} \frac{\rho\sqrt{2}}{2} & \frac{\rho}{2} \\ 0 & \frac{\rho\sqrt{3}}{2} \end{bmatrix} \tag{A6b}$$

where $\rho = \frac{a_P}{a_M}$ is the ratio of the lattice parameter of precipitate to that of matrix.

$$\underline{\underline{A}}^T = \underline{\underline{A}} - I = \begin{bmatrix} \rho\frac{\sqrt{2}}{2} & 0 \\ \frac{\rho}{2} & \frac{\rho\sqrt{3}}{2} \end{bmatrix}\begin{bmatrix} \frac{\rho\sqrt{2}}{2} & \frac{\rho}{2} \\ 0 & \frac{\rho\sqrt{3}}{2} \end{bmatrix} - \begin{bmatrix} 1 & 0 \\ 0 & 1 \end{bmatrix} = \begin{bmatrix} \frac{\rho^2}{2} - 1 & \frac{\rho^2\sqrt{2}}{4} \\ \frac{\rho^2\sqrt{2}}{4} & \rho^2 - 1 \end{bmatrix} \tag{A7}$$

$$[r_1]^2 - [r_2]^2 = \begin{bmatrix} \left(\frac{\rho^2}{2} - 1\right)\cos\theta & \frac{\rho^2\sqrt{2}}{4}\sin\theta \\ \frac{\rho^2\sqrt{2}}{4}\sin\theta & (\rho^2 - 1)\cos\theta \end{bmatrix} \times \begin{bmatrix} \cos\theta \\ \sin\theta \end{bmatrix} \tag{A8}$$

$$\left(\frac{\rho^2}{2} - 1\right)\cos^2\theta + \frac{\rho^2\sqrt{2}}{2}\sin\theta\cos\theta + (\rho^2 - 1)\sin^2\theta = 0 \tag{A9}$$

From the above relationship, the angle between the invariant line and the $[\bar{2}00]$ of matrix can be obtained. To find the similar angle between the invariant line and $[02\bar{2}]$ of the precipitate, the following relationship is used:

$$\begin{bmatrix} \cos\phi \\ \sin\phi \end{bmatrix} = \begin{bmatrix} \frac{\rho\sqrt{2}}{2} & \frac{\rho}{2} \\ 0 & \frac{\rho\sqrt{3}}{2} \end{bmatrix}\begin{bmatrix} \cos\theta \\ \sin\theta \end{bmatrix} \tag{A10}$$

References

1. R. R. HILL and R. ABBASCHIAN, "Physical Metallurgy Principles," 3rd ed. (PWS Publishing, 1991).

2. K. OTSUKA and C. M. WAYMAN, in "Shape Memory Materials," edited by K. Otsuka and C. M. Wayman (Cambridge University Press, Cambridge, UK, 1999) p. 284.
3. T. H. COURTNEY, "Mechanical Behavior of Materials" (McGraw-Hill Inc., 1989).
4. W. BOLLMANN, "Crystal Defects in Crystalline Interfaces" (Springer, Berlin, 1970).
5. P. H. PUMPHREY and K. M. BOWKETT, *Script. Metall.* **5** (1971) 365.
6. D. A. SMITH and R. C. POND, *International Metals Reviews* **205** (1976) 61.
7. U. DAHMEN, P. FERGUSON and K. H. WESTMACOTT, *Acta Metall.* **32** (1984) 803.
8. H. J. FECHT and H. GLEITER, *ibid.* **33** (1985) 557.
9. E. A. LORIA, T. CARNEIRO and H. STUART, in First International Symposium on Structural Intermetallics, edited by R. Darolia *et al.* (TMS, Warrendale, PA, 1993).
10. V. A. SIKKA and E. A. LORIA, *Mat. Sci. Eng*. A **A239–A240** (1997) 745.
11. S. NAKA, M. MARY, M. THOMAS and T. KHAN, *ibid.* **A192–A193** (1995) 69.
12. D. J. SROLOVITZ, M. J. LUTON, R. A. PETKOVIC-LUTON, D. M. BARNETT and W. D. NIX, *Acta Metall.* **32** (1984) 1079.
13. D. J. SROLOVITZ, R. A. PETKOVIC-LUTON and M. J. LUTON, *ibid.* **31** (1983) 1251.
14. J. RÖSSLER and E. ARZT, *ibid.* **38** (1990) 671.
15. E. A. LORIA, *Mat. Sci. Eng.* A **A271** (1999) 430.
16. C. HERRING, *J. Appl. Geophys.* **21** (1950) 437.
17. F. R. N. NABARRO, in "Conference on the Strength of Solids," edited by N. F. Mott (Physical Society, London, 1948) p. 75.
18. R. L. COBLE, *J. Appl. Phys.* **34** (1963) 1979.
19. F. R. N. NABARRO, *Acta. Met.* **37** (1989) 2217.
20. D. BOYNE, Ph.D. thesis, The Ohio State University, 1992.

Received 12 November 2001
and accepted 27 March 2002